





# Defect engineering of hierarchical porous carbon microspheres for potassium-ion storage

Xin-Fei Wu, Zi-Jian Li, Jin-Xiao Liu, Wen Luo\* , Jean-Jacques Gaumet, Li-Qiang Mai 

Received: 16 March 2022 / Revised: 10 April 2022 / Accepted: 12 April 2022  
© Youke Publishing Co., Ltd. 2022

**Abstract** Owing to adjustable microstructure and stable physiochemical properties, carbon-based materials are regarded as promising materials as anodes for potassium-ion batteries (PIBs). Building amorphous structure and introducing defects are favorable methods to generate active sites and improve the electrochemical performances of carbon-based materials. In this work, we develop a facile carbonization method to prepare sulfur-doped amorphous carbon microspheres with hierarchical structure and modulated defects concentration (S-CM-700) for potassium storage. Benefiting from the special microstructure, S-CM-

700 exhibits the optimal performance and obtains high reversible capacity of  $199.6 \text{ mAh}\cdot\text{g}^{-1}$  at  $100 \text{ mA}\cdot\text{g}^{-1}$ , excellent rate property and prominent durability (0.0055% capacity decay per cycle during 1800 cycles). Kinetics analysis and electrochemical characterization are carried out to reveal that the potassium storage could be boosted by regulating the defect level, layer spacing and the content of sulfur-doping. The work provides a general synthesis approach to prepare sustainable carbon anodes for advanced PIBs.

**Keywords** Potassium-ion battery (PIB); Defect engineering; Amorphous carbon; Hierarchical structure; Anode

Xin-Fei Wu and Zi-Jian Li contributed equally to this work.

**Supplementary Information** The online version contains supplementary material available at <https://doi.org/10.1007/s12598-022-02100-3>.

X.-F. Wu, W. Luo\*, L.-Q. Mai  
State Key Laboratory of Advanced Technology for Materials Synthesis and Processing, International School of Materials Science and Engineering, Wuhan University of Technology, Wuhan 430070, China  
e-mail: luowen\_1991@whut.edu.cn

Z.-J. Li, J.-X. Liu, W. Luo, L.-Q. Mai  
State Key Laboratory of Advanced Technology for Materials Synthesis and Processing, School of Materials Science and Engineering, Wuhan University of Technology, Wuhan 430070, China

W. Luo  
Department of Physics, School of Science, Wuhan University of Technology, Wuhan 430070, China

J.-J. Gaumet  
Laboratoire de Chimie et Physique: Approche Multi-échelles, des Milieux Complexes (LCP-A2MC), Institut Jean Barriol, Université de Lorraine, Metz 57070, France

## 1 Introduction

Lithium-ion batteries (LIBs) are widely utilized for electric vehicles and portable electronic devices on account of the outstanding energy density, security, and long working life [1]. Nevertheless, the insufficient lithium precursor reserves and high cost arise great attention to explore sustainable and reliable energy storage technology beyond LIBs [2]. Therefore, potassium-ion batteries (PIBs), with similar energy storage principle to LIBs, are promising alternative to meet these issues. PIBs have attracted attention for low redox potential and cheap precursor [3, 4]. Moreover, compared with  $\text{Li}^+$  and  $\text{Na}^+$ ,  $\text{K}^+$  has the lowest Lewis acidity, making  $\text{K}^+$  exhibit the least interfacial reaction resistance, and the highest ionic mobility and ionic conductivity [5].

Unfortunately, due to the large ionic radius of  $\text{K}^+$  (0.138 vs. 0.068 nm for  $\text{Li}^+$ ), the electrodes often suffer volume



expansion, resulting in poor electrochemical performances during potassiation/depotassiation process [6]. So far, many materials have been developed, including carbon-based materials [7–10], metallic oxides [11], sulfides [12, 13], organic materials [14, 15] and some compounds [16–20]. Carbonaceous materials are considered as the promising and sustainable electrode materials for PIBs, mainly due to low cost, stable physiochemical properties and adjustable microstructure [21, 22]. Graphite can react with  $K^+$  forming  $KC_8$  and along with a theoretical capacity of  $279 \text{ mAh}\cdot\text{g}^{-1}$  [23]. However, the small interlayer spacing of graphite faces failure during  $K^+$  intercalation/deintercalation and eventually results in poor cycle life. Researchers have studied amorphous carbon-based materials which can adapt well to the volume expansion during potassiation/depotassiation process due to the larger interlayer spacing and result in better electrochemical performance. Guo's group fabricated an amorphous ordered mesoporous carbon, showing outstanding electrochemical performance by introducing amorphous mesoporous carbon as alternative anode for PIBs [7]. Yang's group reported the porous amorphous carbon microspheres (PCMs) which delivered high capacity and stability due to large specific surface areas, enlarged interlayer spacings and structural defects from the amorphous character [8]. Therefore, it is a feasible method to boost the electrochemical performance by regulating the crystallinity of carbonaceous materials.

Meanwhile, with regard to further finely regulating microstructure of carbonaceous materials, introducing defects as an effective method has been employed to modulate the surface properties, electronic structures and supply more active sites [24–26]. The defects in carbon-based materials consist of intrinsic defects and extrinsic defects. Intrinsic defects can be divided into vacancies, edges and holes, which are associated with the microstructure. Regulating the preparation of carbon-based materials is a practical method to modify intrinsic defects, including pyrolysis, ball-milling and etching, while extrinsic defects are mostly related to heteroatoms doping [27]. And the synthesis of defect-enriched carbon-based materials is usually not controllable [28]. Hence, it is desirable to develop a facile, controllable and effective way toward large-scale production of advanced carbon anode materials for PIBs.

Herein, we report a facile in situ strategy to prepare amorphous and defect-enriched carbon microspheres with hierarchical structure for potassium storage via pyrolyzing the precursor, iron p-toluene sulfonate ( $(\text{CH}_3\text{C}_6\text{H}_4\text{SO}_3)_3\text{Fe}$ ). By defects engineering, the optimized sample (S-CM-700) with abundant mesopores, plentiful defects and in situ sulfur doping delivers high reversible capacity, great rate performance and prominent

durability. It is found that the amorphous sulfur-doped carbon microspheres (S-CMs) with hierarchical structure support sufficient intrinsic defects and can afford high activity to boost potassium storage. Meanwhile, the results show that the content of defects and in situ S-doping affect the fundamental mechanism of potassiation/depotassiation reactions. By analyzing the  $K^+$  kinetics and storage mechanism of each stage, we provide new insights into the design of sustainable carbonaceous materials for high-performance energy storage devices.

## 2 Experimental

### 2.1 Preparation of S-CMs

$(\text{CH}_3\text{C}_6\text{H}_4\text{SO}_3)_3\text{Fe}$  was purchased from Aladdin and used without further purification. 2 g  $(\text{CH}_3\text{C}_6\text{H}_4\text{SO}_3)_3\text{Fe}$  was calcined at 500, 700 or 900 °C for 2 h under flowing  $\text{N}_2$  with a heating rate of  $5 \text{ }^\circ\text{C}\cdot\text{min}^{-1}$ . The products are, respectively, named as S-CM-500, S-CM-700 and S-CM-900, corresponding to the calcination temperatures. The black-colored products with the solution of 40 ml HCl and 10 ml deionized water were stirred for 1 h. Then, the above solutions were separated by centrifugation and washed three times with deionized water and isopropanol, respectively. The final products were obtained after drying in air atmosphere at 70 °C overnight.

### 2.2 Materials characterizations

Morphologies of the samples were performed via scanning electron microscope (SEM, Phenom Pro microscope) and transmission electron microscope (TEM, JEM-1400). X-ray diffraction (XRD) was measured by a Bruker D8 Discover X-ray diffractometer with  $\text{Cu K}\alpha$  radiation. Raman characterizations were carried out by HORIBA HR EVO Raman system. Fourier transform infrared spectroscopy (FTIR) spectra were recorded by Perkin–Elmer spectrum IR Affinity-1 spectrometer. The Tristar II 3020 instrument was utilized to obtain the surface area and pore-size distribution from nitrogen adsorption at 77 K. The VG Multi Lab 2000 instrument was employed to collect X-ray photoelectron spectroscopic (XPS) spectra. And the elemental analysis was measured by Vario EL cube and rapid OXY cube.

### 2.3 Electrochemical characterizations

Electrochemical performances of S-CMs were evaluated using CR2016 coin-type half-cells. The electrodes were prepared by 80 wt% active materials, 10 wt% acetylene black and 10 wt% carboxymethylcellulose sodium (CMC).

The mixed slurry was coated on Cu foil and dried at 70 °C for at least 10 h. The half cells were assembled in the argon-filled glove box. The counter electrode was potassium foil. And the solution of 0.8 mol·L<sup>-1</sup> potassium hexafluorophosphate (KPF<sub>6</sub>) in ethylene carbon (EC)/diethyl carbonate (DEC) (1:1 in volume ratio) was utilized as electrolyte. Besides, the separator was Whatman glass microfiber (Grade GF/D). Galvanostatic charge–discharge measurement was performed between 0.01 and 3.00 V (vs. K<sup>+</sup>/K) by NEWARE battery testing system. Cyclic voltammetry (CV) was tested in the voltage range of 0.01–3.00 V (vs. K<sup>+</sup>/K) via Autolab PGSTAT302N. Electrochemical impedance spectroscopy (EIS) was evaluated by Autolab PGSTAT302 N.

### 3 Results and discussion

#### 3.1 Morphology and structure

Figure 1 illustrates the synthesis process for the amorphous carbon microspheres with hierarchical structure. The yellowish-colored (CH<sub>3</sub>C<sub>6</sub>H<sub>4</sub>SO<sub>3</sub>)<sub>3</sub>Fe powder is carbonized in flowing N<sub>2</sub> atmosphere at different temperatures to obtain the black-colored S-CMs (namely S-CM-500, S-CM-700, and S-CM-900). As shown in Fig. S1a, the precursor exhibits microspheres with pits and ranges from 5 to 50 μm. The morphology of S-CMs is performed by SEM in Fig. 2a–c. All three samples represent microspheres with hierarchical surface structure, which are made of abundant nanosheets. The unique structure contributes to curtailing the diffusion path of ion and promoting the transfer of interfacial charges [29]. After carbonization at 500 °C, S-CM-500 overall displays a similar microsphere structure inherited from the precursor. In particular, the two-dimensional (2D) nanosheets on the surface have been peeled off and gradually aligned vertically. In Fig. 2b, at 700 °C, the skeleton of 3D structure becomes more prominent. And from Fig. 2d (SEM image of the peripheral edge of S-CM-700), the nanosheets on the surface are completely aligned

vertically. As illustrated in Fig. 2c, at 900 °C, the structure of microspheres shrinks and collapses, making it difficult to maintain the spherical morphology, forming an irregular polyhedral structure, and some microspheres are collapsed. For further analyzing the fracture section, Fig. S1b, c shows that the fracture surface presents jagged dendritic micron structure. Figure 2e, f shows TEM images of S-CM-700. It can be observed that the central part of the microspheres represents solid and dense feature, while the peripheral edge part of the microspheres is in vertical growth of nanosheet structure with a relatively thin thickness. In addition, the folded and twisted nanosheet structure can be clearly seen.

To further characterize the structure of S-CMs, XRD and Raman spectroscopy were measured. As shown in XRD patterns (Fig. 3a), the as-synthesized samples display two broad diffraction peaks at about 20° and 43°, which are assigned to the crystallographic planes of (002) and (100), respectively [30, 31]. The two broad diffraction peaks demonstrate the amorphous structure. According to the Bragg's equation, *d*-spacings (*d*<sub>002</sub>) of the as-synthesized samples are calculated to be 0.408, 0.415, 0.409 nm, respectively (Table 1). S-CM-700 exhibits the largest interlayer spacings, and the large interlayer spacing contributes to alleviating volume expansion and maintaining structural stability during potassiation/depotassiation process, which is favorable for the storage of K<sup>+</sup> [32]. In the Raman spectra (Fig. 3b), the peaks centered around 1345 and 1600 cm<sup>-1</sup> are associated with the defects induced D-band and the graphite crystallites of carbon generated G-band, respectively [33]. The area ratio of D-band to G-band (*I*<sub>D</sub>/*I*<sub>G</sub>) can be utilized to reflect the disordered degree and abundance of defects in carbon-based materials [34–36]. As shown in Table 1, *I*<sub>D</sub>/*I*<sub>G</sub> of S-CM-500, S-CM-700, S-CM-900 is 3.23, 2.40 and 1.10, respectively. And the decreased ratios indicate that the degree of graphitization increases with the calcination temperature, which is consistent with XRD results in Fig. 3a. In addition, *I*<sub>D</sub>/(*I*<sub>D</sub> + *I*<sub>G</sub>) represents the measure of defects. The values of S-CM-500, S-CM-700 and S-CM-900 are 0.76, 0.71 and

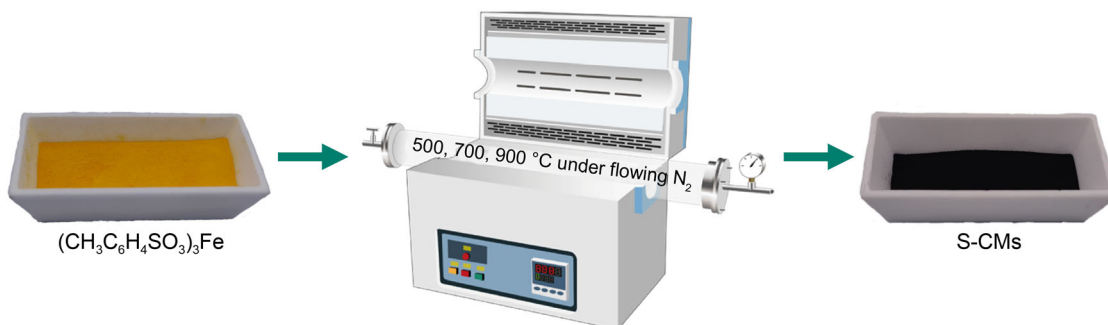
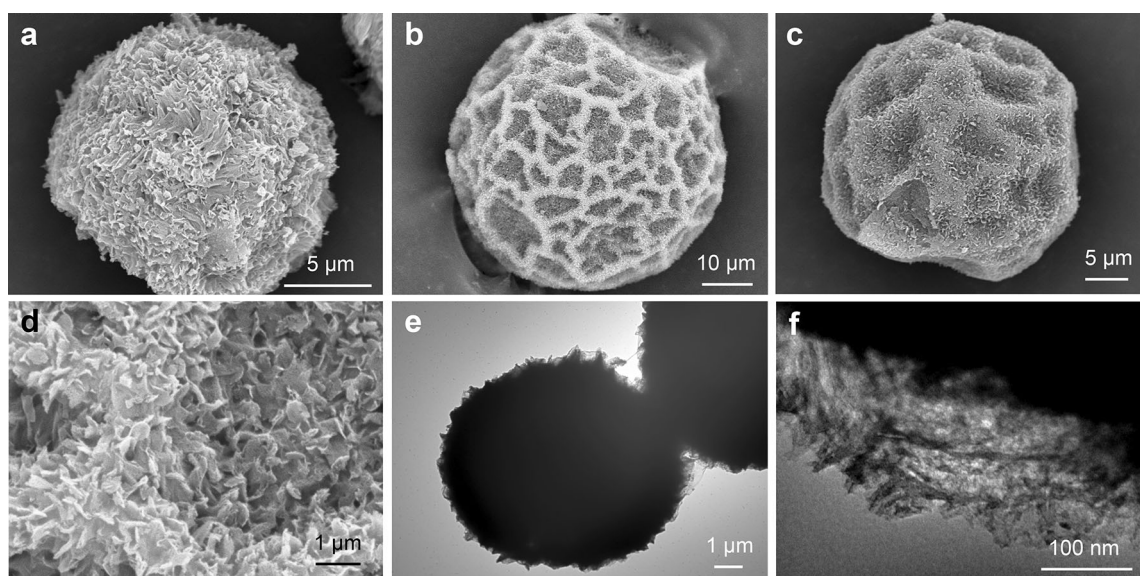
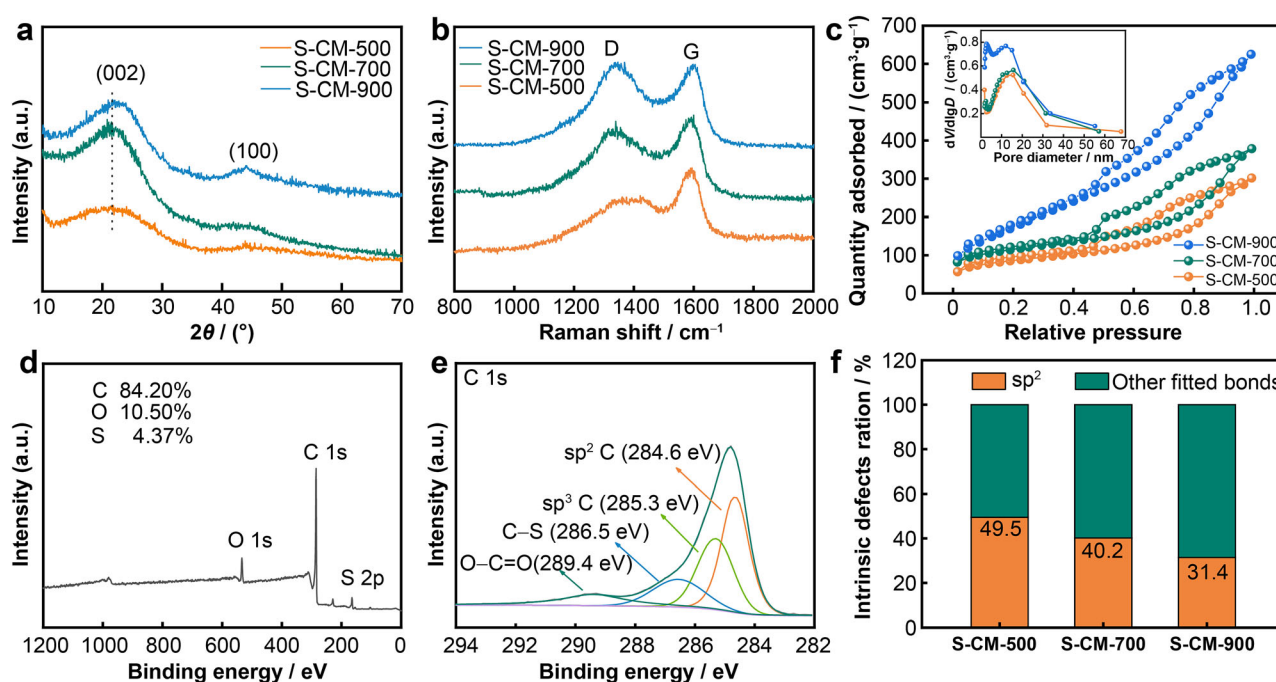


Fig. 1 Illustration of synthesis process of S-CMs



**Fig. 2** SEM images of **a** S-CM-500, **b** S-CM-700 and **c** S-CM-900; **d** SEM image of peripheral edge of S-CM-700; **e** TEM image of S-CM-700; **f** TEM image of peripheral edge of S-CM-700



**Fig. 3** **a** XRD patterns, **b** Raman spectra, **c** N<sub>2</sub> adsorption–desorption isotherms and (inset) corresponding pore size distribution of S-CM-500 (orange), S-CM-700 (green) and S-CM-900 (blue); **d** full-spectrum XPS survey and **e** C 1s XPS spectra of S-CM-700; **f** ratios of C-sp<sup>2</sup> and other fitted bonds of S-CMs

0.52, respectively, further confirming that the degree of graphitization increases and defect level decreases with the carbonization temperature. This shows that the amorphous carbon with more defects and disorders, which is obtained by lower temperature treatment, may be able to serve as active sites and is expected to provide better electrochemical performance [8, 11]. Meanwhile, FTIR

measurement was carried out to investigate the structures. As present in Fig. S2, after carbonization, most of the original absorption peaks of (CH<sub>3</sub>C<sub>6</sub>H<sub>4</sub>SO<sub>3</sub>)<sub>3</sub>Fe disappear, and only a weak peak can be displayed at around 1385 cm<sup>-1</sup>, which is related to the stretching vibrations of C–S band [5]. It is indicated that during the pyrolysis process, the original organic groups were decomposed, and

**Table 1** Physical properties of S-CMs

Samples	$d_{002}$ / nm	$I_D/I_G$	$I_D/(I_D + I_G)$	BET surface area / ( $\text{m}^2 \cdot \text{g}^{-1}$ )	Elemental analysis				
					$w_C$ / wt%	$w_H$ / wt%	$w_O$ / wt%	$w_S$ / wt%	$w_S/w_O$
S-CM-500	0.408	3.23	0.76	303.56	71.10	2.63	7.30	14.04	1.92
S-CM-700	0.415	2.40	0.71	403.11	75.94	2.46	5.08	14.17	2.79
S-CM-900	0.409	1.10	0.52	666.49	79.98	2.43	6.51	9.55	1.47

most of S in the sulfonic acid group finally existed in the carbonized products in the form of C–S bond, which also confirms the successful in situ doping of sulfur.

To determine the evolution of the surface area and pore structure, nitrogen adsorption–desorption was surveyed. According to Fig. 3c, all isotherms display typical Type IV behavior, demonstrating the mesoporous structure [37]. The Brunauer–Emmett–Teller (BET) surface areas of S-CM-500, S-CM-700 and S-CM-900 are 303.56, 403.11 and 666.49  $\text{m}^2 \cdot \text{g}^{-1}$ , respectively. Since the functional groups related to heteroatoms such as O and S can enhance the wettability of carbon, which can significantly improve the contact area between electrolyte and carbon surface [38–40], with the increase in calcination temperature and specific surface area, the active sites (such as defects and S-rich functional groups) existing on the carbon nanosheets have been sufficiently exposed, and the potassium-ion adsorption sites and reaction sites on the surface have been improved [41]. Figure 3c also displays the pore size distribution of the three samples. The result reveals that the pore structure of the three samples is mainly mesoporous, which is consistent with the curves of nitrogen adsorption–desorption. The existence of mesopores for S-CM-700 can accelerate electrolyte infusion, alleviate the volume expansion and promote the ion transmission efficiency during the potassiation/depotassiation process [7]. The large specific surface area and hierarchical porous structure not only shorten the transport distance of potassium ion, but also provide multiple active sites for fast potassium capacitive adsorption [38–40].

To analyze the surface chemical state and chemical composition, the calcined materials were examined by XPS. Compared with the survey XPS spectrum of S-CM-700 in Fig. 3d, all the samples (Figs. S3, S4) exhibit three elements C, O and S. For C 1s spectra of S-CM-700 in Fig. 3e, four peaks at 284.6, 285.3, 286.5 and 289.4 eV are related to C- $\text{sp}^2$ , C- $\text{sp}^3$ , C–S and O–C=O bonds [34, 42], respectively. The C- $\text{sp}^2$  bonds are related to the inherent defects [25], and its ratio to other carbon bonds in Fig. 3f displays that the amount of its inherent defects gradually decreases as the calcination temperature increases. The defect content of S-CM-500 and S-CM-700 is much higher

than that of S-CM-900, which can provide additional  $\text{K}^+$ -storage sites. The S 2p spectra (Fig. S5a) of S-CM-700 exhibit three peaks corresponding to S 2 $p_{3/2}$  (164.0 eV), S 2 $p_{1/2}$  (165.2 eV) and  $-\text{C}-\text{SO}_2-$  (168.9 eV) [43]. The S 2 $p_{3/2}$  and S 2 $p_{1/2}$  peaks can be divided to thiophene-type sulfur and the  $-\text{C}-\text{SO}_2-$  peak can be assigned to oxidized-type sulfur [41]. And researchers found that thiophene-type S can optimize the electronic structure, decrease the adsorption energy of  $\text{K}^+$  during potassiation/depotassiation and promote  $\text{K}^+$  diffusion kinetics [43]. For O 1s spectra of S-CM-700 in Fig. S5b, it can be deconvoluted into O–S at 531.5 eV, along with C=O at 533.1 eV, C–OH at 534.1 eV and COOH at 535.1 eV [30, 44], respectively. By elemental analysis, S-CM-700 processes the highest S content and the lowest O content. Besides, the S/O weight ratios of S-CM-500, S-CM-700 and S-CM-900 are 1.92, 2.79 and 1.47, respectively (Table 1). And the elemental analysis result is consistent with XPS composition of S-CMs (Table S1). Some previous studies have confirmed that the S/O ratio is related to the potassium storage performance [43, 45]. A higher S/O ratio of S-CM-700 is beneficial to reduce the side reactions and proportion of irreversible capacity.

### 3.2 Potassium-storage performance

The potassium-storage performance of S-CMs has an intimate relationship with the specific structure at different temperatures. Figure 4a exhibits the short-term cycling properties of S-CMs at 100  $\text{mA} \cdot \text{g}^{-1}$ . The reversible capacity of S-CM-700 can remain 199.6  $\text{mAh} \cdot \text{g}^{-1}$ , which is much higher than those of S-CM-500 (78.2  $\text{mAh} \cdot \text{g}^{-1}$ ) and S-CM-900 (142.0  $\text{mAh} \cdot \text{g}^{-1}$ ). The initial Coulombic efficiency (ICE) is calculated to be 33.9% (S-CM-500), 35.4% (S-CM-700) and 24.2% (S-CM-900), respectively. All the S-CMs demonstrate low ICE, which is associated with the high specific surface area and oxygen-contained groups, promoting the formation of solid electrolyte interphase (SEI) membrane [46, 47]. And this phenomenon is often observed for carbon-based anode materials in PIBs [25, 37]. Therefore, S-CM-900 with the largest specific surface possesses the lowest ICE. After the carbon material

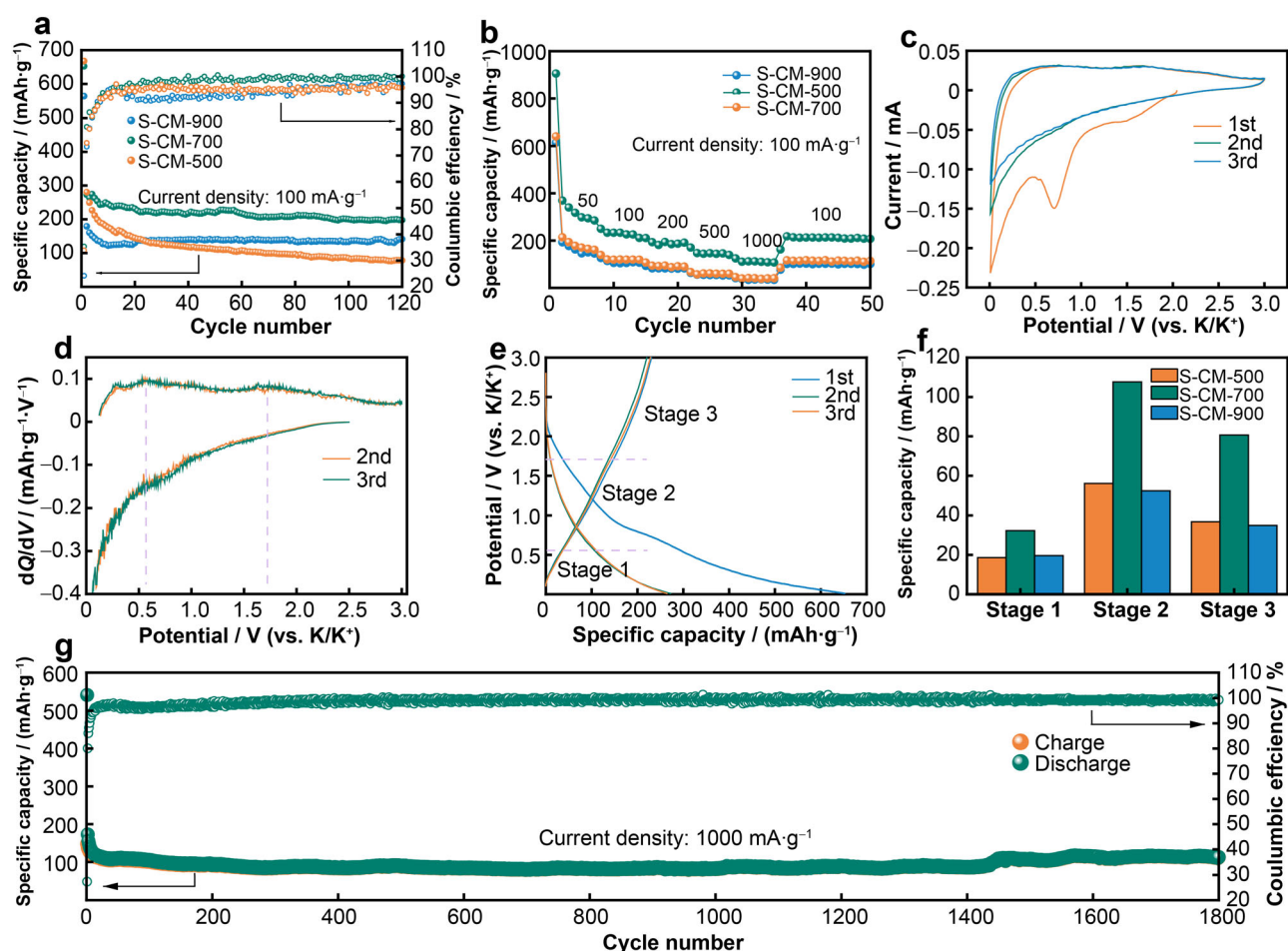


**Fig. 4** Electrochemical potassium storage performances for anodes: **a** cycling performance at a current density of 100 mA·g<sup>-1</sup>, **b** rate performances of S-CMs; **c** CV curves of S-CM-700 at a scan rate of 0.1 mV·s<sup>-1</sup>; **d** differential capacity curves of S-CM-700 for the second and third cycles at a current density of 100 mA·g<sup>-1</sup>; **e** electrochemical charge/discharge profiles of S-CM-700 for the first three cycles at a current density of 100 mA·g<sup>-1</sup>; **f** specific capacity at each stage of the second cycle charging process for S-CMs at a current density of 100 mA·g<sup>-1</sup>; **g** long cycling performance at a current density of 1000 mA·g<sup>-1</sup> of S-CM-700

and its functional groups are stabilized through the activation process, the Coulombic efficiency (CE) of S-CM-700 can reach about 100%, always higher than those of S-CM-500 and S-CM-900 during the cycle process. This result can be attributed to the side reactions from the excess oxygen containing functional groups in S-CM-500 (S/O wt%: 1.92) and S-CM-900 (S/O wt%: 1.47). Besides, although S-CM-500 reveals the most degree of defects, it displays disappointed electrochemical performance, which can be contributed to its smaller layer spacing and more irreversible reactions from lower S/O ratio. While undesirable electrochemical performance of S-CM-900 is due to its low defect content, which is incapable to provide sufficient reaction active sites, and the small interlayer spacing makes it difficult to intercalate large K<sup>+</sup>. S-CM-700 with the largest layer spacing, the highest S/O ratio and plentiful defects provide the highest reversible specific capacity,

which is also verified in Fig. 4b. S-CM-700 delivers reversible specific capacities of 308.6, 220.5, 176.6, 131.7, 96.7 mAh·g<sup>-1</sup> at 50, 100, 200, 500, 1000 mA·g<sup>-1</sup>, respectively. Moreover, when the current density is restored 100 mA·g<sup>-1</sup>, S-CM-700 regains reversible specific capacity of 218.1 mAh·g<sup>-1</sup> and the capacity retention is up to 98.9%. Significantly, S-CM-700 shows outstanding rate performance, reversibility and cycling stability. In contrast, for each current density, the other two anodes display much lower capacities than S-CM-700. These results indicate S-CM-700 anodes possess an impressive capacity and great rate performance. To further understand the excellent K<sup>+</sup> storage properties, SEM and TEM images (Fig. S6a, b) of S-CM-700 anodes have been characterized after 220 cycles at 50 mA·g<sup>-1</sup>. As shown in Fig. S6a, b, the hierarchical microspheres microstructure of S-CM-700 anodes still can be observed after cycles, revealing the highly reversibility.

Figures 4c, S7a and S7c reveal CV curves of S-CMs at  $0.1 \text{ mV}\cdot\text{s}^{-1}$ . During the initial potassiation cycle of all samples, an irreversible peak appears near 0.7 V, which is related to the irreversible reaction between  $\text{K}^+$  and the functional groups and the formation of SEI [48]. S-CM-900 has the highest specific surface area, so its irreversible peak is the most obvious, which is confirmed by its lowest ICE [49]. In the case of S-CM-700, a pair of reversible redox CV peaks appear at 0.78 and 1.75 V, corresponding to the reversible capture of  $\text{K}^+$  at S-containing functional group sites [43]. The cathodic peak about 0.01 V can be the intercalation of  $\text{K}^+$  in S-CM-700 [34]. The apparent overlap in the subsequent CV cycles reflects great reversibility of S-CM-700.

The potassium-storage mechanism of S-CM-700 can be explored through the charge–discharge of S-CM-700 at  $100 \text{ mA}\cdot\text{g}^{-1}$  and their corresponding differential capacity curves, which can show the decayed intensity and the increased potential difference of the redox peaks. As shown in Fig. 4d, S-CM-700 presents two anodic peaks at 0.54 and 1.75 V, related to the dividing line between the different stages of the discharging–charging curves in Fig. 4e. Based on this, the charging curves can be segmented into three regions, which coincide with three different stages for the interaction between potassium ion and anode materials [6, 25, 50]. The potassium storage mechanisms of S-CM-700 in the three stages are attributed to  $\text{K}^+$  deintercalation behavior enabled by short range ordered carbon units (Stage 1), the redox reaction between  $\text{K}^+$  and S-containing functional groups (Stage 2), as well as the desorption of  $\text{K}^+$  from mesopores and defects (Stage 3), respectively [25]. The capacity comparison provided by different stages is intuitively shown in Fig. 4f. S-CM-700 has excellent potassium storage in each stage, which is related to its appropriate defect concentration, the largest layer spacing and moderate specific surface area. Specifically, S-CM-900 treated under the highest carbonization temperature has the most short-range ordered carbon micro-regions, so the capacity provided in Stage 1 is higher than that of S-CM-500 [7]. However, since the layer spacings of S-CM-500 and S-CM-900 are smaller than that of S-CM-700, the deintercalation of  $\text{K}^+$  in the two materials is more difficult, so the electrochemical performance of S-CM-500 and S-CM-900 is disappointed [32]. S-CM-700 has the highest S content, so it provides the highest capacity in Stage 2. On the contrary, S-CM-900 has the lowest S content, so it shows the lowest capacity for redox reaction with  $\text{K}^+$ . S-CM-500 has higher defect concentration, so it shows higher capacity than S-CM-900 in Stage 3, but also worse than S-CM-700 due to its lower specific surface area and smaller layer spacing [25]. As shown in Figs. 4e, S7b and S7d, the charge–discharge curves show the same voltage

platform for S-CMs, indicating the potassium-storage mechanism of mesoporous carbon is similar.

In order to further test the cycle stability of S-CM-700 at high current density, the long-term cycling test was measured at  $1000 \text{ mA}\cdot\text{g}^{-1}$  (Fig. 4g). The reversible capacities of the 10th and 1800th cycles are 125.6 and 113.1  $\text{mAh}\cdot\text{g}^{-1}$ , respectively. After the activation process, S-CM-700 presents excellent durability and a high-capacity retention of 90.1%, which means that it shows only 0.0055% capacity decay in each cycle. Therefore, S-CM-700 exhibits an excellent stable reversibility.

For distinguishing the charge storage mechanism, the kinetics and electrochemical reaction of  $\text{K}^+$  in S-CM-700 were further investigated. A series of CV measurements were performed at different scan rates from 0.2 to  $1.0 \text{ mV}\cdot\text{s}^{-1}$  (Fig. 5a). At different scanning rates, the redox peaks of CV curves have no obvious distortion, indicating that the polarization effects are weak [51]. The current ( $i$ ) and scan rate ( $v$ ) can be expressed by the formular [52]:

$$i = av^b \quad (1)$$

where  $a$  and  $b$  are constants. According to the above formula, the slope  $b$ -value can directly reflect the control factors of  $\text{K}^+$  storage. The  $b$ -value close to 1 corresponds a surface capacitive-controlled process. And it can be described as a diffusion-limited process when the  $b$ -value is close to 0.5 [52]. By employing the maximum (peak) current, the  $b$ -values calculated from the anode peaks and cathode peaks of S-CM-700 are 0.87 and 0.91, respectively (Fig. 5b), indicating that the  $\text{K}^+$  storage is controlled not only by surface capacitive-controlled process, but also by diffusion-limited process. The defects and S-rich functional groups introduced by S atoms on the carbon surface bring additional adsorption sites, so as to strengthen the capacitance control process and help to accelerate the electrochemical reaction kinetics [51, 53–55].

Figures 5c, S8 exhibit the  $\text{K}^+$  diffusivity ( $D_{\text{K}^+}$ ) of S-CMs by galvanostatic intermittent titration technique (GITT). The  $D_{\text{K}^+}$  of S-CMs can be calculated by Fick's second law [56], and that of S-CM-700 is from  $2.06 \times 10^{-12}$  to  $3.42 \times 10^{-10} \text{ cm}^2\cdot\text{s}^{-1}$ . The samples at all temperatures have high  $D_{\text{K}^+}$ , indicating that S-CMs present fast  $\text{K}^+$ -diffusion kinetics [37]. Figure 5d shows EIS curves of S-CM-700 anodes at different cycles. And the corresponding equivalent circuit diagram is analyzed in Fig. S9a [57, 58]. As shown in Table S2, after several cycles, the resistance of SEI film ( $R_{\text{SEI}}$ ) remained at a stable value, representing the stability of SEI membrane, which can enhance the transfer of  $\text{K}^+$  in the electrolyte and electrode interface [44]. Meanwhile, the charge transfer resistance ( $R_{\text{ct}}$ ) becomes lower, improving the charge transfer of potassium ion [41]. And in Fig. S9b, EIS measurements of S-CMs after one cycle were also

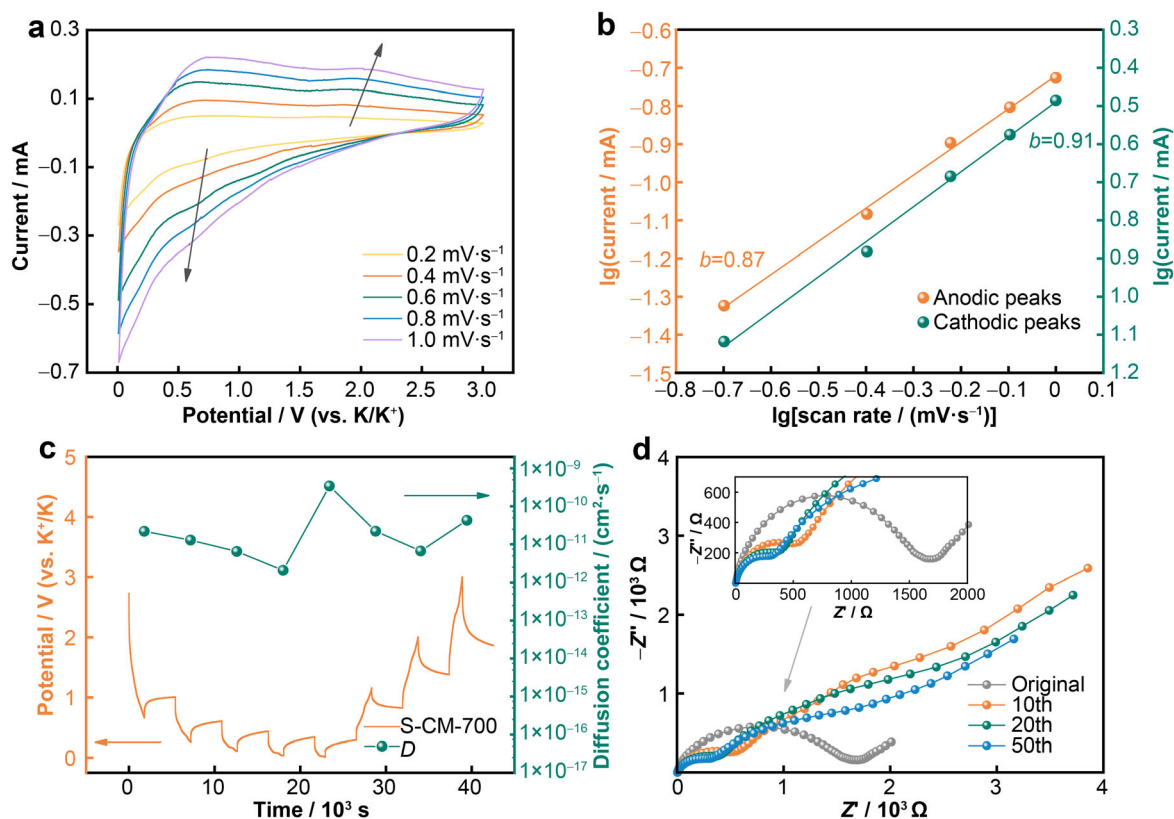


**Fig. 5** Kinetics analysis for S-CM-700: **a** CV curves from 0.2 to 1.0  $\text{mV}\cdot\text{s}^{-1}$ , **b** corresponding  $b$ -values plotted for anodic peaks and cathodic peaks; **c** GITT profiles and corresponding  $\text{K}^+$  diffusion coefficients; **d** Nyquist impedance plots after different cycles, where  $Z'$  is real part of impedance and  $Z''$  is imaginary part of impedance

operated, and equivalent circuit diagram and resistance value are analyzed in Fig. S9a and Table S3, respectively. Obviously, S-CM-700 shows the lowest  $R_{\text{SEI}}$  and  $R_{\text{ct}}$ , which is conducive to kinetics of potassium-ion transmission, consistent with its remarkable electrochemical performance.

## 4 Conclusion

To sum up, low-cost precursor (iron p-toluene sulfonate) was carbonized in one step, and S-CMs microspheres with hierarchical structure were obtained. The as-synthesized S-CM-700 has plentiful defects, the largest layer spacing, the richest sulfur content and moderate specific surface area. The excellent potassium-storage performance of S-CM-700 is coincided with its specific structure. Specifically, as the anode of PIBs, S-CM-700 presents great reversible capacity ( $199.6 \text{ mAh}\cdot\text{g}^{-1}$  at  $100 \text{ mA}\cdot\text{g}^{-1}$ ), impressive durability (0.0055% capacity attenuation in each cycle over 1800 cycles) and good rate property. Further, the capacity contribution dominated by surface capacitive-controlled was determined. This study provides

an effective way for advanced battery system to develop excellent carbon-based anode materials.

**Acknowledgements** This work was financially supported by the National Natural Science Foundation of China (No. 51904216), the State Key Laboratory of Advanced Technology for Materials Synthesis and Processing (No. WUT: 2022-KF-4) and the National Innovation Training Program for College Students (No. 312040000254).

## Declarations

**Conflicts of interests** The authors declare that they have no conflict of interest.

## References

- [1] Tarascon JM, Armand M. Issues and challenges facing rechargeable lithium batteries. *Nature*. 2001;414(6861):359. <https://doi.org/10.1038/35104644>.
- [2] Zhang WC, Lu J, Guo ZP. Challenges and future perspectives on sodium and potassium ion batteries for grid-scale energy storage. *Mater Today*. 2021;50:400. <https://doi.org/10.1016/j.mattod.2021.03.015>.
- [3] Zhang W, Liu Y, Guo Z. Approaching high-performance potassium-ion batteries via advanced design strategies and



- engineering. *Sci Adv.* 2019;5(5):eaav7412. <https://doi.org/10.1126/sciadv.aav7412>.
- [4] Zhou M, Wang Q, Yuan Y, Luo SH, Zhang YH, Liu X. Bio-carbon with different microstructures derived from corn husks and their potassium storage properties. *Rare Met.* 2021;40(11):3166. <https://doi.org/10.1007/s12598-021-01775-4>.
- [5] Liu Y, Tai Z, Zhang J, Pang WK, Zhang Q, Feng H, Konstantinov K, Guo Z, Liu HK. Boosting potassium-ion batteries by few-layered composite anodes prepared via solution-triggered one-step shear exfoliation. *Nat Commun.* 2018;9(1):3645. <https://doi.org/10.1038/s41467-018-05786-1>.
- [6] Qian Y, Li Y, Yi Z, Zhou J, Pan Z, Tian J, Wang Y, Sun S, Lin N, Qian Y. Revealing the double-edged behaviors of heteroatom sulfur in carbonaceous materials for balancing K-storage capacity and stability. *Adv Funct Mater.* 2021;31(8):2006875. <https://doi.org/10.1002/adfm.202006875>.
- [7] Wang W, Zhou J, Wang Z, Zhao L, Li P, Yang Y, Yang C, Huang H, Guo S. Short-range order in mesoporous carbon boosts potassium-ion battery performance. *Adv Energy Mater.* 2018;8(5):1701648. <https://doi.org/10.1002/aenm.201701648>.
- [8] Chen M, Wang W, Liang X, Gong S, Liu J, Wang Q, Guo SJ, Yang H. Sulfur/oxygen codoped porous hard carbon microspheres for high-performance potassium-ion batteries. *Adv Energy Mater.* 2018;8(19):1800171. <https://doi.org/10.1002/aenm.201800171>.
- [9] Xu Z, Du S, Yi Z, Han J, Lai C, Xu Y, Zhou X. Water chestnut-derived slope-dominated carbon as a high-performance anode for high-safety potassium-ion batteries. *ACS Appl Energy Mater.* 2020;3(11):11410. <https://doi.org/10.1021/acsaem.0c02327>.
- [10] Han X, Guo X, Xu M, Pang H, Ma Y. Clean utilization of palm kernel shell: sustainable and naturally heteroatom-doped porous activated carbon for lithium-sulfur batteries. *Rare Met.* 2020;39(9):1099. <https://doi.org/10.1007/s12598-020-01439-9>.
- [11] Zhang Q, Didier C, Pang WK, Liu Y, Wang Z, Li S, Peterson VK, Mao J, Guo Z. Structural insight into layer gliding and lattice distortion in layered manganese oxide electrodes for potassium-ion batteries. *Adv Energy Mater.* 2019;9(30):1900568. <https://doi.org/10.1002/aenm.201900568>.
- [12] Guo Y, Zhang L, Xi Li D, Kang J. Advances of carbon materials as loaders for transition metal oxygen/sulfide anode materials. *Chin J Rare Met.* 2021;45(10):1241. <https://doi.org/10.13373/j.cnki.cjrm.XY20040016>.
- [13] Du Y, Weng W, Zhang Z, He Y, Xu J, Sun J, Liao J, Bao J, Zhou X. Candied-Haws-like architecture consisting of FeS<sub>2</sub>@C core-shell particles for efficient potassium storage. *ACS Mater Lett.* 2021;3(4):356. <https://doi.org/10.1021/acsmaterialslett.1c00129>.
- [14] Lei Z, Yang Q, Xu Y, Guo S, Sun W, Liu H, Lv LP, Zhang Y, Wang Y. Boosting lithium storage in covalent organic framework via activation of 14-electron redox chemistry. *Nat Commun.* 2018;9(1):576. <https://doi.org/10.1038/s41467-018-02889-7>.
- [15] Li SY, Li WH, Wu XL, Tian Y, Yue J, Zhu G. Pore-size dominated electrochemical properties of covalent triazine frameworks as anode materials for K-ion batteries. *Chem Sci.* 2019;10(33):7695. <https://doi.org/10.1039/c9sc02340b>.
- [16] Zhang WC, Pang WK, Sencadas V, Guo ZP. Understanding high-energy-density Sn<sub>4</sub>P<sub>3</sub> anodes for potassium-ion batteries. *Joule.* 2018;2(8):1534. <https://doi.org/10.1016/j.joule.2018.04.022>.
- [17] Liao J, Chen C, Hu Q, Du Y, He Y, Xu Y, Zhang Z, Zhou X. A low-strain phosphate cathode for high-rate and ultralong cycle-life potassium-ion batteries. *Angew Chem Int Ed Engl.* 2021;60(48):25575. <https://doi.org/10.1002/anie.202112183>.
- [18] Han J, Zhu K, Liu P, Si Y, Chai Y, Jiao L. N-doped CoSb@C nanofibers as a self-supporting anode for high-performance K-ion and Na-ion batteries. *J Mater Chem A.* 2019;7(44):25268. <https://doi.org/10.1039/c9ta09643d>.
- [19] Liu Y, Zhang N, Jiao L, Tao Z, Chen J. Ultrasmall Sn nanoparticles embedded in carbon as high-performance anode for sodium-ion batteries. *Adv Funct Mater.* 2015;25(2):214. <https://doi.org/10.1002/adfm.201402943>.
- [20] Luo XX, Li WH, Liang HJ, Zhang HX, Du KD, Wang XT, Liu XF, Zhang JP, Wu XL. Covalent organic framework with highly accessible carbonyls and pi-cation effect for advanced potassium-ion batteries. *Angew Chem Int Ed Engl.* 2022;61(10):e202117661. <https://doi.org/10.1002/anie.202117661>.
- [21] Rajagopalan R, Tang YG, Ji XB, Jia CK, Wang HY. Advancements and challenges in potassium ion batteries: a comprehensive review. *Adv Funct Mater.* 2020;30(12):1909486. <https://doi.org/10.1002/adfm.201909486>.
- [22] Bin C, Li X. Recent progress on carbon-based anode materials for Na-ion batteries. *Acta Phys Chim Sin.* 2020;36(5):1905003. <https://doi.org/10.3866/PKU.WHXB201905003>.
- [23] Fan L, Ma R, Zhang Q, Jia X, Lu B. Graphite anode for a potassium-ion battery with unprecedented performance. *Angew Chem Int Ed Engl.* 2019;58(31):10500. <https://doi.org/10.1002/anie.201904258>.
- [24] Olsson E, Cottom J, Cai Q. Defects in hard carbon: where are they located and how does the location affect alkaline metal storage? *Small.* 2021;17(18):e2007652. <https://doi.org/10.1002/sml.202007652>.
- [25] Huang R, Zhang X, Qu Z, Zhang X, Lin J, Wu F, Chen R, Li L. Defects and sulfur-doping design of porous carbon spheres for high-capacity potassium-ion storage. *J Mater Chem A.* 2022;10(2):682. <https://doi.org/10.1039/d1ta09337a>.
- [26] Olsson E, Chai G, Dove M, Cai Q. Adsorption and migration of alkali metals (Li, Na, and K) on pristine and defective graphene surfaces. *Nanoscale.* 2019;11(12):5274. <https://doi.org/10.1039/c8nr10383f>.
- [27] Zhu JW, Mu SC. Defect engineering in the carbon-based electrocatalysts: insight into the intrinsic carbon defects. *Adv Funct Mater.* 2020;30(25):2001097. <https://doi.org/10.1002/adfm.202001097>.
- [28] Xiao L, Lu H, Fang Y, Sushko ML, Cao Y, Ai X, Yang H, Liu J. Low-defect and low-porosity hard carbon with high coulombic efficiency and high capacity for practical sodium ion battery anode. *Adv Energy Mater.* 2018;8(20):1703238. <https://doi.org/10.1002/aenm.201703238>.
- [29] Ding S, Zhang D, Chen JS, Lou XW. Facile synthesis of hierarchical MoS<sub>2</sub> microspheres composed of few-layered nanosheets and their lithium storage properties. *Nanoscale.* 2012;4(1):95. <https://doi.org/10.1039/c1nr11552a>.
- [30] Peng Y, Chen Z, Zhang R, Zhou W, Gao P, Wu J, Liu H, Liu J, Hu A, Chen X. Oxygen-containing functional groups regulating the carbon/electrolyte interfacial properties toward enhanced K<sup>+</sup> storage. *Nanomicro Lett.* 2021;13(1):192. <https://doi.org/10.1007/s40820-021-00722-3>.
- [31] Wang Z, Feng X, Bai Y, Yang H, Dong R, Wang X, Xu H, Wang Q, Li H, Gao H, Wu C. Probing the energy storage mechanism of quasi-metallic Na in hard carbon for sodium-ion batteries. *Adv Energy Mater.* 2021;11(11):2003854. <https://doi.org/10.1002/aenm.202003854>.
- [32] Cai C, Chen Y, Hu P, Zhu T, Li X, Yu Q, Zhou L, Yang X, Mai L. Regulating the interlayer spacings of hard carbon nanofibers enables enhanced pore filling sodium storage. *Small.* 2022;18(6):e2105303. <https://doi.org/10.1002/sml.202105303>.
- [33] Hou BH, Wang YY, Ning QL, Li WH, Xi XT, Yang X, Liang HJ, Feng X, Wu XL. Self-supporting, flexible, additive-free, and scalable hard carbon paper self-interwoven by 1D microbelts:

- superb room/low-temperature sodium storage and working mechanism. *Adv Mater.* 2019;31(40):e1903125. <https://doi.org/10.1002/adma.201903125>.
- [34] Zhang Y, Li L, Xiang Y, Zou G, Hou H, Deng W, Ji X. High sulfur-doped hard carbon with advanced potassium storage capacity via a molten salt method. *ACS Appl Mater Interfaces.* 2020;12(27):30431. <https://doi.org/10.1021/acsami.0c07616>.
- [35] Damodar D, Ghosh S, Rani MU, Martha SK, Deshpande AS. Hard carbon derived from sepals of Palmyra palm fruit calyx as an anode for sodium-ion batteries. *J Power Sources.* 2019;438:227008. <https://doi.org/10.1016/j.jpowsour.2019.227008>.
- [36] Shi MM, Bao D, Li SJ, Wulan BR, Yan JM, Jiang Q. Anchoring PdCu amorphous nanocluster on graphene for electrochemical reduction of N<sub>2</sub> to NH<sub>3</sub> under ambient conditions in aqueous solution. *Adv Energy Mater.* 2018;8(21):1800124. <https://doi.org/10.1002/aenm.201800124>.
- [37] Sun Y, Wang H, Wei W, Zheng Y, Tao L, Wang Y, Huang M, Shi J, Shi ZC, Mitlin D. Sulfur-rich graphene nanoboxes with ultra-high potassiation capacity at fast charge: storage mechanisms and device performance. *ACS Nano.* 2021;15(1):1652. <https://doi.org/10.1021/acsnano.0c09290>.
- [38] Yan SX, Wang Q, Luo SH, Zhang YH, Liu X, Liu YG, Wang ZY, Hao AM, Yi TF. Coal-based S hybrid self-doped porous carbon for high-performance supercapacitors and potassium-ion batteries. *J Power Sources.* 2020;461:228151. <https://doi.org/10.1016/j.jpowsour.2020.228151>.
- [39] Liu X, Tong Y, Wu Y, Zheng J, Sun Y, Niu L, Li H. Synergistically enhanced electrochemical performance using nitrogen, phosphorus and sulfur tri-doped hollow carbon for advanced potassium ion storage device. *Chem Eng J.* 2022;431:133986. <https://doi.org/10.1016/j.cej.2021.133986>.
- [40] Zhao GY, Yu DF, Zhang H, Sun FF, Li JW, Zhu L, Sun L, Yu M, Besenbacher F, Sun Y. Sulphur-doped carbon nanosheets derived from biomass as high-performance anode materials for sodium-ion batteries. *Nano Energy.* 2020;67:104219. <https://doi.org/10.1016/j.nanoen.2019.104219>.
- [41] Yao QQ, Gan YM, Ma ZJ, Qian XY, Cai SZ, Zhao Y, Guan LH, Huang W. Approaching superior potassium storage of carbonaceous anode through a combined strategy of carbon hybridization and sulfur doping. *Energy Environ Mater.* 2021. <https://doi.org/10.1002/eem2.12217>.
- [42] Hu K, Qin L, Zhang S, Zheng J, Sun J, Ito Y, Wu Y. Building a reactive armor using S-doped graphene for protecting potassium metal anodes from oxygen crossover in K–O<sub>2</sub> batteries. *ACS Energy Lett.* 2020;5(6):1788. <https://doi.org/10.1021/acsenrgylett.0c00715>.
- [43] Li JL, Qin W, Xie JP, Lei H, Zhu YQ, Huang WY, Xu X, Zhao ZJ, Mai WJ. Sulphur-doped reduced graphene oxide sponges as high-performance free-standing anodes for K-ion storage. *Nano Energy.* 2018;53:415. <https://doi.org/10.1016/j.nanoen.2018.08.075>.
- [44] Tao L, Yang YP, Wang HL, Zheng YL, Hao HC, Song WP, Shi J, Huang MH, Mitlin D. Sulfur-nitrogen rich carbon as stable high capacity potassium ion battery anode: performance and storage mechanisms. *Energy Storage Mater.* 2020;27:212. <https://doi.org/10.1016/j.ensm.2020.02.004>.
- [45] Li Z, Wu X, Luo W, Wang C, Feng W, Hong X, Mai L. Dual sulfur-doped sites boost potassium storage in carbon nanosheets derived from low-cost sulfonate. *Chem Eng J.* 2022;431:134207. <https://doi.org/10.1016/j.cej.2021.134207>.
- [46] Ding J, Zhang H, Zhou H, Feng J, Zheng X, Zhong C, Paek E, Hu W, Mitlin D. Sulfur-grafted hollow carbon spheres for potassium-ion battery anodes. *Adv Mater.* 2019;31(30):1900429. <https://doi.org/10.1002/adma.201900429>.
- [47] Qian Y, Jiang S, Li Y, Yi Z, Zhou J, Tian J, Lin N, Qian YT. Understanding mesopore volume-enhanced extra-capacity: optimizing mesoporous carbon for high-rate and long-life potassium-storage. *Energy Storage Mater.* 2020;29:341. <https://doi.org/10.1016/j.ensm.2020.04.026>.
- [48] Zuo Y, Li P, Zang R, Wang S, Man Z, Li P, Wang S, Zhou W. Sulfur-doped flowerlike porous carbon derived from metal-organic frameworks as a high-performance potassium-ion battery anode. *ACS Appl Energy Mater.* 2021;4(3):2282. <https://doi.org/10.1021/acsaem.0c02799>.
- [49] Liang HJ, Hou BH, Li WH, Ning QL, Yang X, Gu ZY, Nie XJ, Wang G, Wu XL. Staging Na/K-ion de-/intercalation of graphite retrieved from spent Li-ion batteries: in operando X-ray diffraction studies and an advanced anode material for Na/K-ion batteries. *Energy Environ Sci.* 2019;12(12):3575. <https://doi.org/10.1039/C9EE02759A>.
- [50] Xiao W, Sun Q, Banis MN, Wang B, Li W, Li M, Lushington A, Li R, Li X, Sham TK, Sun X. Understanding the critical role of binders in phosphorus/carbon anode for sodium-ion batteries through unexpected mechanism. *Adv Funct Mater.* 2020;30(32):2000060. <https://doi.org/10.1002/adfm.202000060>.
- [51] Wang D, Tian KH, Wang J, Wang ZY, Luo SH, Liu YG, Wang Q, Zhang YH, Hao AM, Yi TF. Sulfur-doped 3D hierarchical porous carbon network toward excellent potassium-ion storage performance. *Rare Met.* 2021;40(9):2464. <https://doi.org/10.1007/s12598-021-01715-2>.
- [52] Augustyn V, Come J, Lowe MA, Kim JW, Taberna PL, Tolbert SH, Abruña HD, Simon P, Dunn B. High-rate electrochemical energy storage through Li<sup>+</sup> intercalation pseudocapacitance. *Nat Mater.* 2013;12(6):518. <https://doi.org/10.1038/NMAT3601>.
- [53] Sun MJ, Qu YH, Zeng FY, Yang Y, Xu K, Yuan CL, Lu ZH. Hierarchical porous and sandwich-like sulfur-doped carbon nanosheets as high-performance anodes for sodium-ion batteries. *Ind Eng Chem Res.* 2022;61(5):2126. <https://doi.org/10.1021/acs.iecr.1c04575>.
- [54] Wang G, Shao M, Ding H, Qi Y, Lian J, Li S, Qiu J, Li H, Huo F. Multiple active sites of carbon for high-rate surface-capacitive sodium-ion storage. *Angew Chem Int Ed Engl.* 2019;58(38):13584. <https://doi.org/10.1002/anie.201908159>.
- [55] Liang HJ, Gu ZY, Zheng XY, Li WH, Zhu LY, Sun ZH, Meng YF, Yu HY, Hou XK, Wu XL. Tempura-like carbon/carbon composite as advanced anode materials for K-ion batteries. *J Energy Chem.* 2021;59:589. <https://doi.org/10.1016/j.jechem.2020.11.039>.
- [56] Tang K, Yu X, Sun J, Li H, Huang X. Kinetic analysis on LiFePO<sub>4</sub> thin films by CV, GITT, and EIS. *Electrochim Acta.* 2011;56(13):4869. <https://doi.org/10.1016/j.electacta.2011.02.119>.
- [57] Luo W, Gaumet JJ, Magri P, Diliberto S, Li F, Franchetti P, Ghanbaja J, Mai L. Fast, green microwave-assisted synthesis of single crystalline Sb<sub>2</sub>Se<sub>3</sub> nanowires towards promising lithium storage. *J Energy Chem.* 2019. <https://doi.org/10.1016/j.jechem.2018.03.013>.
- [58] Tian S, Guan D, Lu J, Zhang Y, Liu T, Zhao X, Yang C, Nan J. Synthesis of the electrochemically stable sulfur-doped bamboo charcoal as the anode material of potassium-ion batteries. *J Power Sources.* 2020. <https://doi.org/10.1016/j.jpowsour.2019.227572>.